# Supplementary Information

## Section 1: S1. Detailed information about the installed instruments

As can be seen in **Figure 1**, stainless steel lines pass through the manifolds to sample air from the chamber to instruments alongside, and in the laboratory above the MAC. Ground floor instruments include all standard gas and particle instruments that are routinely connected to the chamber along with those that would be affected adversely by sampling losses or artefacts, and several instruments specifically for the BB experiments. Routine measurements include $NO_2$, NO, NOx, $O_3$, CO, total particle number concentration and particle number size distribution. These were supplemented by $CO_2$ and $CH_4$ for the BB experiments, along with the iodide ion chemical ionisation time-of-flight mass spectrometer with the filter inlet for gases and aerosols (FIGAERO-$I^-$-ToF-CIMS), in addition to the particle sample collection for offline chemical measurement. The other instruments were in the first-floor of the laboratory subsampling from a line drawing air from the chamber via a nafion drier. One subsampling line was connected to a charge neutraliser (Kr-85then via a flow splitter to mobility size selection for measurement of monodisperse particle hygroscopicity under sub-saturated or supersaturated conditions (using a hygroscopicity tandem differential mobility analyser, HTDMA and cloud condensation nucleus counter, CCNc, respectively). Sample air from the second line passed alternately to a thermodenuder or a bypass line via a three-way valve to a suite of instruments measuring physical, chemical and optical properties of the particles (scanning mobility particle sizer, SMPS; Aerodyne Aerosol Mass Spectrometer, AMS; DMT single particle soot photometer, SP2; and 3-wavelength photo-acoustic soot spectrometer, PASS). Sampling was automatically controlled to sequentially measure un-denuded and denuded air with programmed temperature steps.

### S.1.1. Aerosol Mass Spectrometer (AMS)

The composition and mass of non-refractory aerosols (organic, sulfate, nitrate, ammonium and chloride) is analysed using a variety of optional online mass spectrometers, most routinely the Aerodyne compact time-of-flight AMS (CR-ToF-AMS, ARI Inc., USA; Drewnick et al., 2005), with a sampling rate of ~0.1 L/min. The AMS is calibrated using mobility-size-selected ammonium nitrate and ammonium sulfate particles, following established procedures by Jimenez et al., (2003) and Allan et al., (2004). For the 2 example campaigns presented in the current manuscript, the average ionization efficiency of ammonium nitrate was determined to be 5.2 x 10-7 and 4.535 x 10-7 ions/molecule in April and September respectively. Through ion balance assessments of ammonium nitrate and ammonium sulfate in these calibrations, specific relative ionization efficiencies (RIEs) were established for NH4+ and SO42- as 4.3556 and 1.0888, respectively. For all organic compounds, the RIEs were set to the default value of 1.4 (Alfarra et al., 2004).

### S.1.2. Single Particle Soot Photometer (SP2)

The concentrations and mixing state of refractory black carbon (BC) are characterised using a Droplet Measurement Technologies SP2. The SP2 can detect BC-containing particles with an equivalent spherical diameter in the range of 70–850 nm (Liu et al., 2014). Briefly, when a BC-containing particle passes through an intra-cavity Nd:YAG laser beam (at $\lambda$ = 1064 nm), the BC absorbs the laser and heats up. On reaching its boiling temperature, it will incandesce and emit

visible light. The SP2 incandescence signal is proportional to the mass of refractory BC present in the particle. The derived BC mass can be then converted to a spherical equivalent BC core diameter ($D_C$), using an assumed density of 1.8 g $cm^{-3}$. The SP2 incandescence signal is calibrated using Aquadag BC particle standards, which follows the calibration procedures in Laborde et al. (2012). The SP2 can also provide the mixing state (coating) of BC-containing particles by determining the light-scattering signals at $\lambda = 1064$ nm. The scattering signal is processed using a leading edge only (LEO) method to reconstruct the distorted scattering signal when BC-containing particles transit through the laser beam and cause coating loss from laser heating (Gao et al., 2007). The LEO methodology is described in detail in previous studies (Liu et al., 2014; Taylor et al., 2015). The scattering channel is calibrated using polystyrene latex spheres (PSLs) at 300 nm. A Mie core–shell model is employed to interpret the diameter of BC-containing particles ($D_P$) and hence the shell/core ratios ($D_P/D_C$) (Taylor et al., 2015).

### S.1.3. Hygroscopic Tandem Differential Mobility Analyser (HTDMA)

A custom-built HTDMA (Good et al., 2010a; Wang Y et al 2022) is used to measure size-selected particle hygroscopicity under subsaturated conditions. Briefly, it comprises a first DMA to size-select dried particles, a humidifier, a second DMA to size the humidified particles and a water-based Condensation Particle Counter (CPC). Dry size selection, humidification (here held at 90% RH) and wet sizing are sequenced automatically. The second DMA stepped through 24 sizes with selected growth factor (GF) ranging from 0.75-2.6 (GF defined as wet diameter divided by the initial selected dry size; $D_{p,wet}/D_{p,dry}$) in 10 s steps requiring 8 minutes total.

In each campaign reported here, two HTDMA calibrations were conducted before and mid-campaign, including DMA sizing using monodisperse PSLs and humidity calibration using nebulized ammonium sulphate using its well-defined hygroscopicity behavior.

### S.1.4. Cloud Condensation Nucleus counter (CCNc)

A Droplet Meaurement Technologies continuous flow streamwise thermal gradient CCNc (Roberts and Nenes, 2005; Wang Y et al 2022) is used to measure water affinity of monodisperse submicron particles under supersaturated condition providing a measurement of particle hygroscopicity by evaluation of their ability to be activated as cloud droplets. Upstream dried and charge neutralized particle size selection used a Vienna type long DMA (type: Finnish Vienna Long) and synchronous counting of particles of all dry sizes was conducted using a butanol-based TSI CPC model 3775 to enable the activated fraction ($F_A$) of particles to be calculated at each size. The selected dry particle diameter stepped from 20 nm to 517 nm across 10 minutes, synchronised with each setpoint supersaturation on the CCNc, which was in turn stepped from 0.1%, 0.2%, 0.3%, 0.4%, 0.5% (Values set in the CCNC PC program before measurements, i.e. non corrected or calibrated SS values) with an additional 10 minutes to stabilise when reducing from the highest supersaturation back to 0.1%, resulting in a 60 minutes cycle. Sigmoidal fitting to the calculated $F_A$ at all sizes enables derivation of the dry diameter for activation (D50)

Calibration of the DMPS-CCNC coupling is routinely conducted with PSLs and ammonium sulphate, for DMA particle size and CCNc supersaturation (SS) respectively (Good, N., et al., 2010; Rose, D., et al. 2008, Irwin, M. et al. 2010).

### S.1.5. Chemical Ionisation Mass Spectrometer (CIMS)

A high resolution-time-of-flight CIMS (HR-ToF-CIMS; Lee et al., 2014) is operated to obtain continuous (online) gas-phase measurements using Iodide (I-) as reagent ion. Iodide is produced by passing methyl iodide ($CH_3I$) and ultra-high purity (UHP) $N_2$ over a $^{210}Po$ radioactive source and directly introduced into the ion-molecule region (IMR). As detailed by Junninen et al. (2010), the reduced pressure IMR (100 mbar) is coupled to a Tofwerk atmospheric pressure interface high-resolution time-of-flight mass spectrometer (APi-ToF). A full description of the instrument has been previously provided by Priestley et al. (2018a, b). Gas-phase sampling from the chamber is done using a PTFE tube (1/4-inch i.d.) at 2 L/min. "Instrument background" measurements are obtained by intermittently flushing the instrument with UHP $N_2$ during the measurements.

### S.1.6. Filter Sampling and Offline Analysis

Two particle filter sampling approaches are used. The first is a custom-made filter constructed to fit the chamber exhaust system collecting all particles remaining in the chamber at the end of experiment, as described in Shao et al (2022). Filters collected from the chamber have been twice diluted. Two Pall in-Line 47mm filter holders fitted with polycarbonate filters are additionally connected to a vacuum line with a mass flow controller (MFC) sampling at 2 L/min (Evans, R. L., et al, 2024) after the first stage dilution. Locations of the samplers are illustrated in Figure 1. The filtered particles may be subjected to a variety of offline analyses.

# Section 2: List of the experiments of the first biomass burning campaign (April and September 2022) at University of Manchester

**Table S1. List of the experiments of the first biomass burning campaign (April and September 2023) at University of Manchester**

| Experiment names | Experiment codes | Experiment dates | Fuel types (source) | Burning Condition | Measurement condition |
|---|---|---|---|---|---|
| 20220411-softwood-flaming | NP-F-SW | 11/04/2022 | Softwood (2) | Flaming | Non-photoaging |
| 20220407-softwood-flaming | F-SW-1 | 07/04/2022 | Softwood (2) | Flaming | Photoaging |
| 20220413-softwood-flaming | F-SW-2 | 13/04/2022 | Softwood (2) | Flaming | Photoaging |
| 20220901-softwood-flaming | F-SW-3 | 01/09/2022 | Softwood (3) | Flaming | Photoaging |
| 20220406-softwood-smouldering | NP-F-SW | 06/04/2022 | Softwood (1) | Smouldering | Non-photoaging |
| 20220408-softwood-smouldering | S-SW-1 | 08/04/2022 | Softwood (2) | Smouldering | Photoaging |
| 20220906-softwood-smouldering | S-SW-2 | 06/09/2022 | Softwood (3) | Smouldering | Photoaging |
| 20220915-softwood-smouldering | S-SW-3 | 15/09/2022 | Softwood (3) | Smouldering | Photoaging |
| 20220422-hardwood-flaming | NP-F-HW-1 | 22/04/2022 | Hardwood(1) | Flaming | Non-photoaging |
| 20220429-hardwood-flaming | NP-F-HW-2 | 29/04/2022 | Hardwood(1) | Flaming | Non-photoaging |
| 20220421-hardwood-flaming | F-HW-1 | 21/04/2022 | Hardwood(1) | Flaming | Photoaging |
| 20220428-hardwood-flaming | F-HW-2 | 28/04/2022 | Hardwood(1) | Flaming | Photoaging |
| 20220830-hardwood-flaming | F-HW-3 | 30/08/2022 | Hardwood(2) | Flaming | Photoaging |
| 20220922-hardwood-flaming | HF_P_4 | 22/09/2022 | Hardwood(2) | Flaming | Photoaging |
| 20220419-hardwood-smouldering | NP-S-HW-1 | 19/04/2022 | Hardwood(1) | Smouldering | Non-photoaging |
| 20220427-hardwood-smouldering | NP-S-HW-2 | 27/04/2022 | Hardwood(1) | Smouldering | Non-photoaging |
| 20220414-hardwood-smouldering | S-HW-1 | 14/04/2022 | Hardwood(1) | Smouldering | Photoaging |
| 20220420-hardwood-smouldering | S-HW-2 | 20/04/2022 | Hardwood(1) | Smouldering | Photoaging |
| 20220426-hardwood-smouldering | S-HW-3 | 26/04/2022 | Hardwood(1) | Smouldering | Photoaging |
| 20220831-hardwood-smouldering | S-HW-4 | 31/08/2022 | Hardwood(2) | Smouldering | Photoaging |
| 20220916-leaves | L_1 | 16/09/2022 | Leaves | Smouldering | Photoaging |
| 20220929-leaves | L_2 | 29/09/2022 | Leaves | Smouldering | Photoaging |

| | | | | | |
|---|---|---|---|---|---|
| 20220913-leaves | L_3 | 13/09/2022 | Leaves | Smouldering | Photoaging |
| 20220926-leaves | L_4 | 26/09/2022 | Leaves | Smouldering | Photoaging |
| 20220927-leaves | L_5 | 27/09/2022 | Leaves | Smouldering | Photoaging |
| 20220914-peat | P_1 | 28/09/2022 | Peat | Smouldering | Photoaging |
| 20220921-peat | P_2 | 21/09/2022 | Peat | Smouldering | Photoaging |
| 20220928-peat | P_3 | 14/09/2022 | Peat | Smouldering | Photoaging |

## Section 3: S3. Additional Figures for the Experimental Results

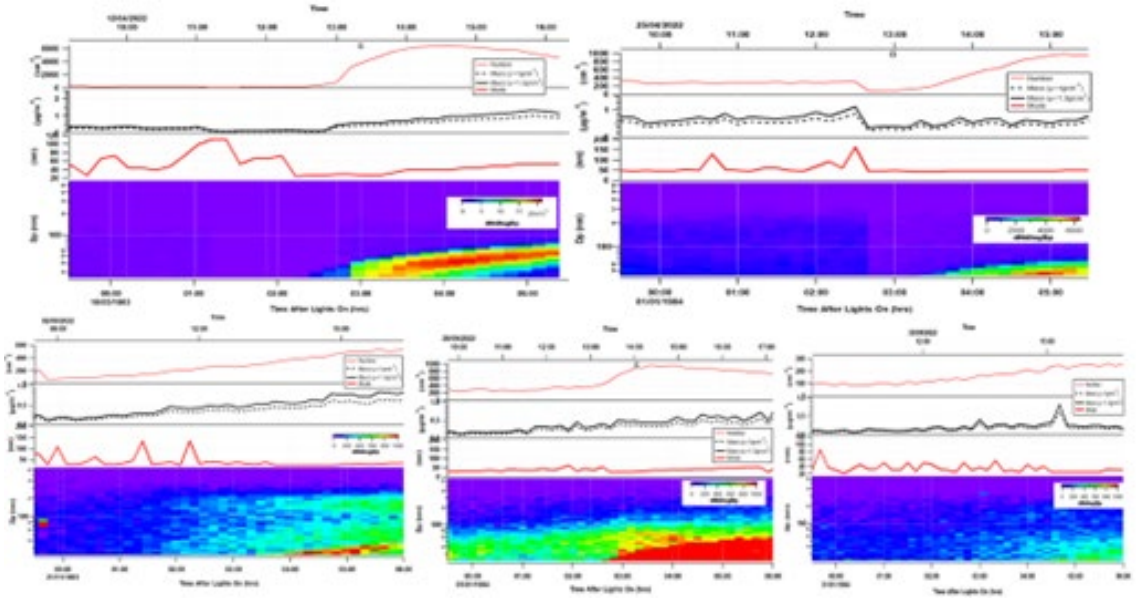

**Fig. S1. DMPS particle size distribution of background experiments**

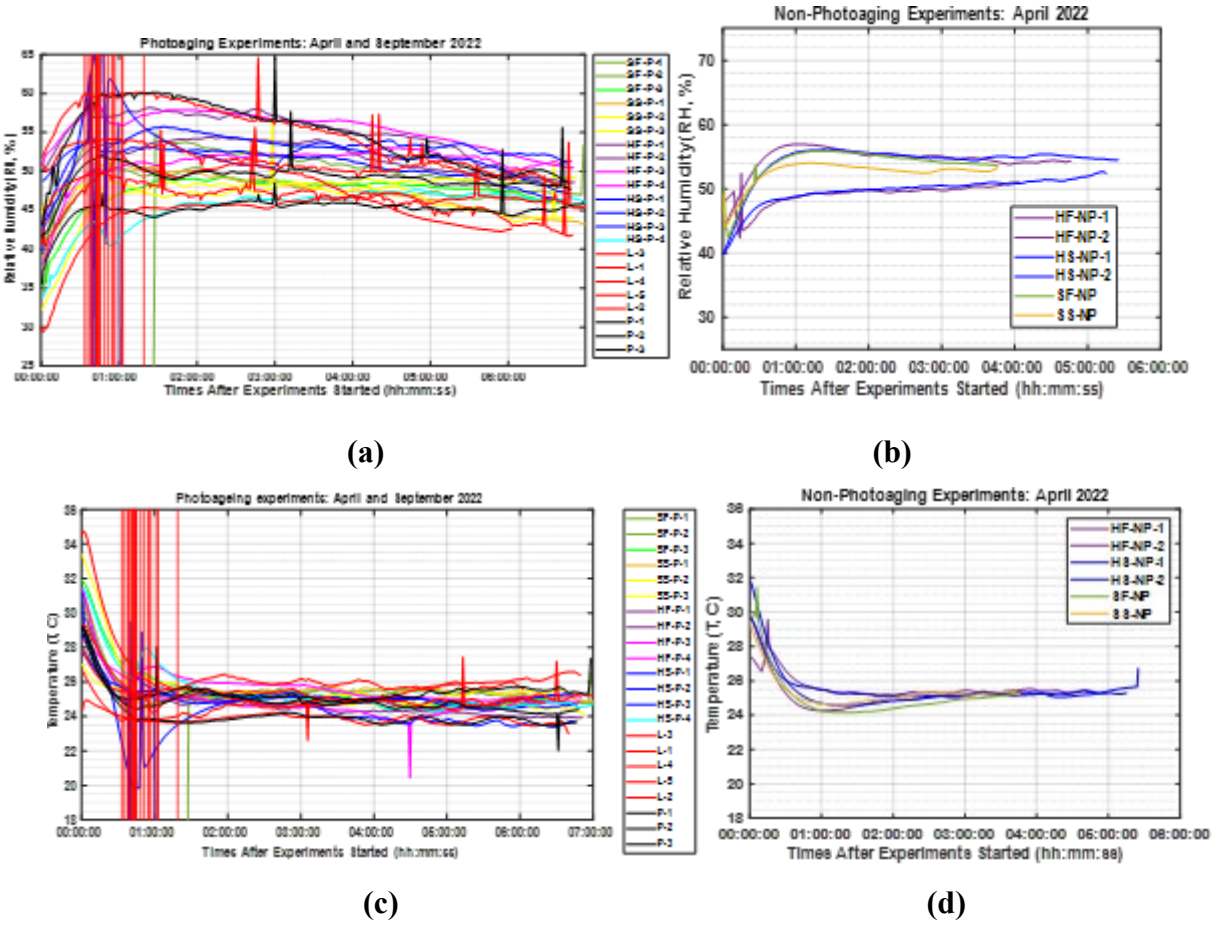


**Figure S2.** RH and temperature graphs in photo-ageing **(a, c)** and non-photo-ageing **(b, d);** vertical red lines indicate the initial times of the lights on

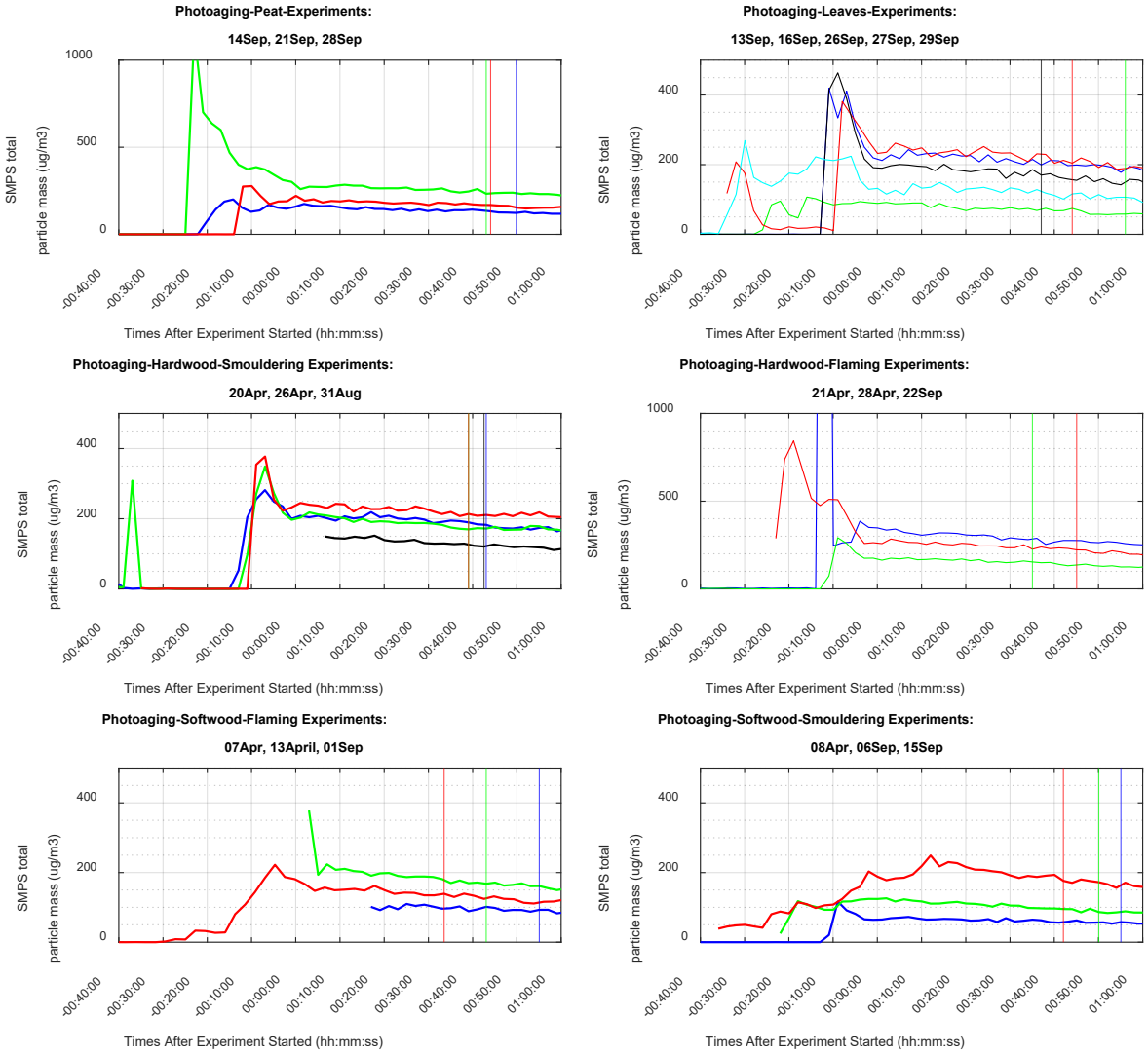
Photoaging-Peat-Experiments:
14Sep, 21Sep, 28Sep
Photoaging-Leaves-Experiments:
13Sep, 16Sep, 26Sep, 27Sep, 29Sep
Photoaging-Hardwood-Smouldering Experiments:
20Apr, 26Apr, 31Aug
Photoaging-Hardwood-Flaming Experiments:
21Apr, 28Apr, 22Sep
Photoaging-Softwood-Flaming Experiments:
07Apr, 13April, 01Sep
Photoaging-Softwood-Smouldering Experiments:
08Apr, 06Sep, 15Sep
SMPS total particle mass (ug/m3)
Times After Experiment Started (hh:mm:ss)
-00:40:00
-00:30:00
-00:20:00
-00:10:00
00:00:00
00:10:00
00:20:00
00:30:00
00:40:00
00:50:00
01:00:00

**(a)**

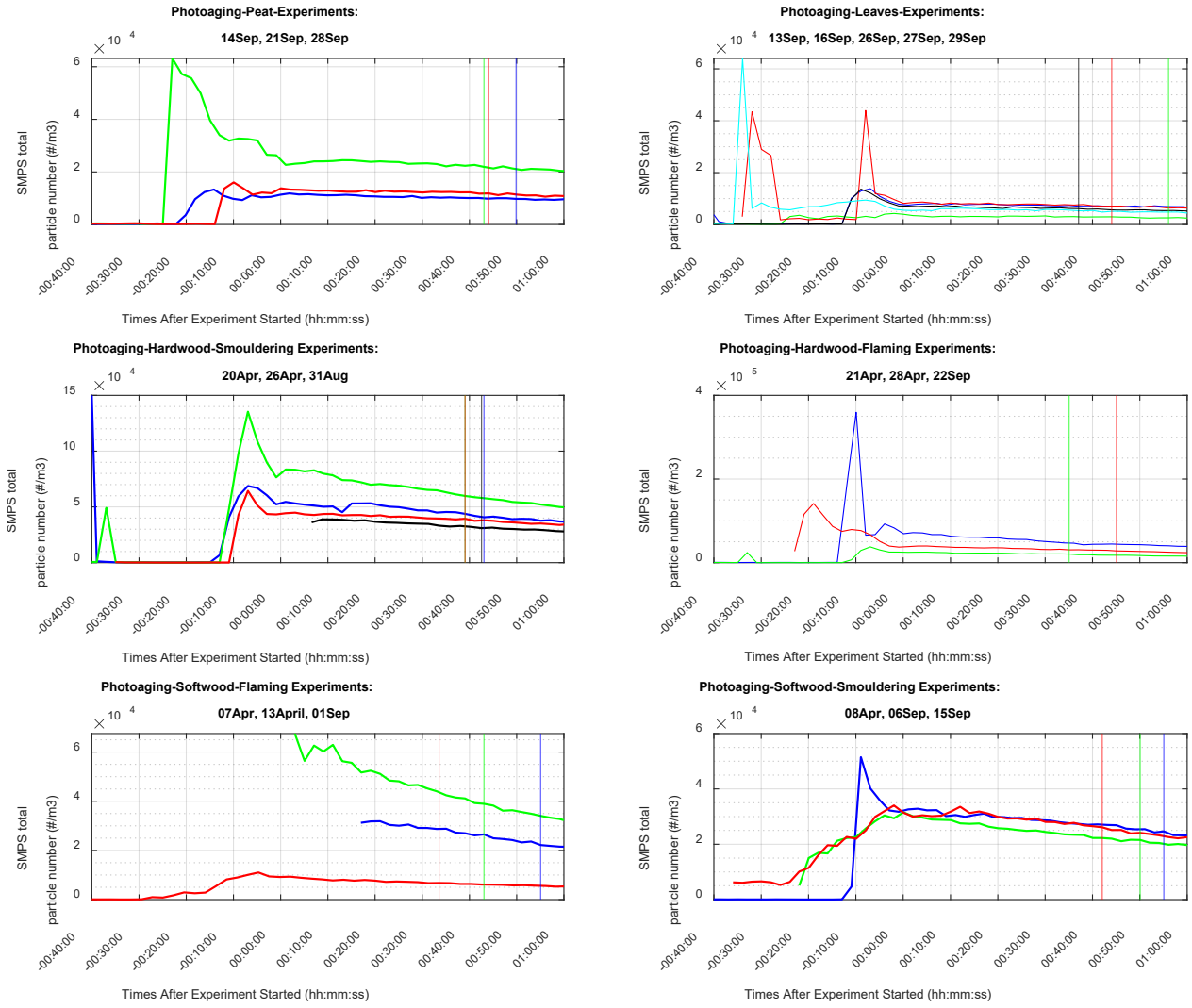


(**b**)

**Fig. S3**. SMPS total particle mass concentration **(a)** and SMPS total particle number concentration **(b)**; vertical red lines indicate the initial times of the lights on. Each color in each panel just means a different repetition.

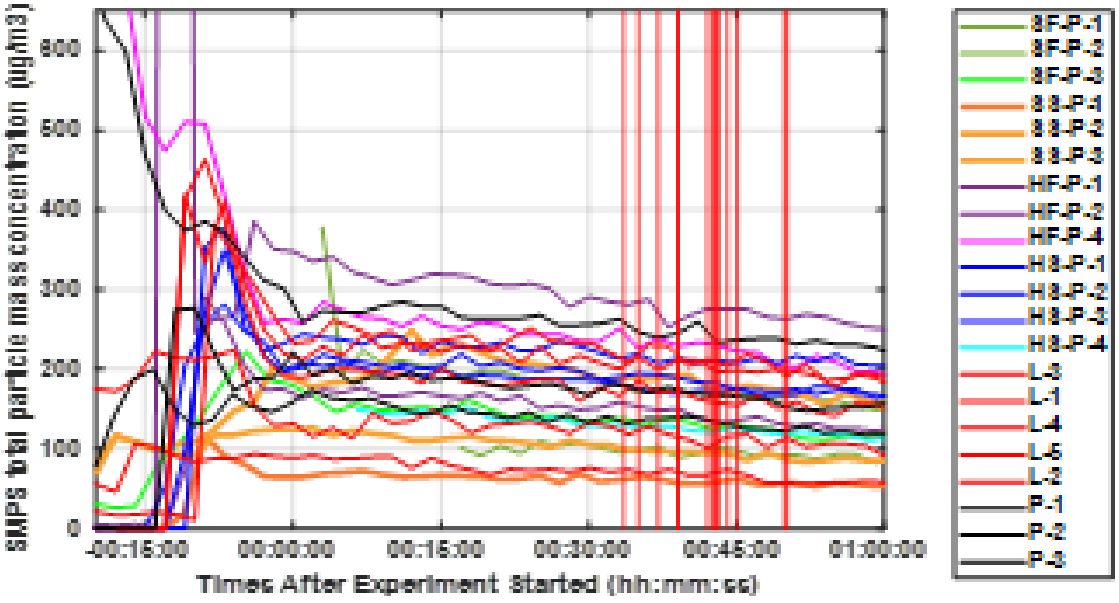


**(a)**

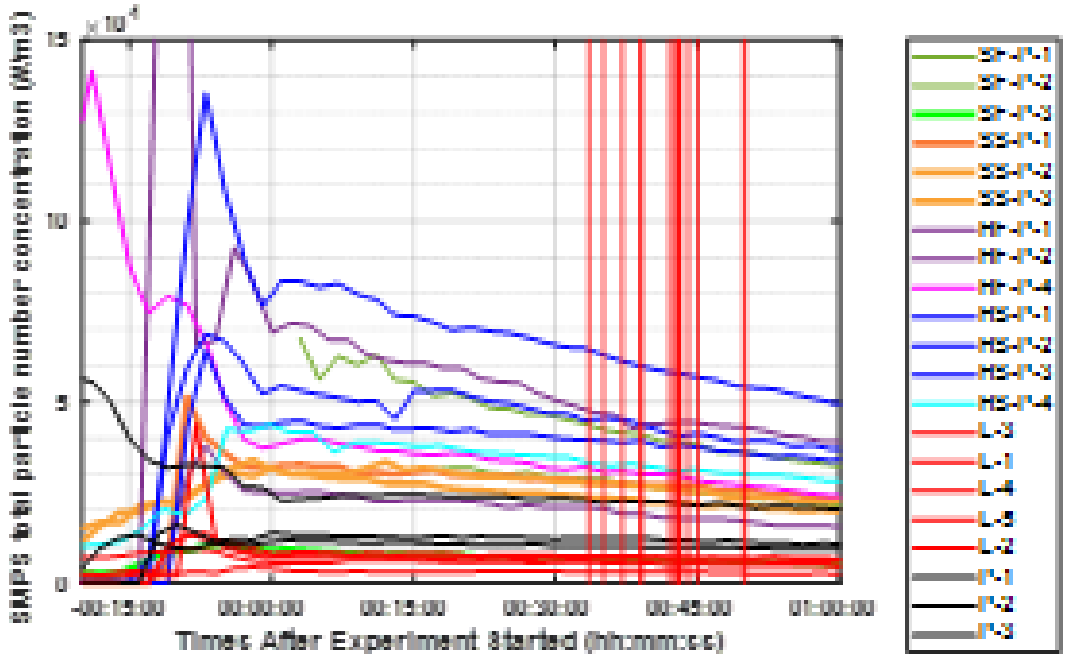


**(b)**

**Fig. S4.** SMPS total particle mass concentration (a) and SMPS total particle number concentration (b); vertical red lines indicate the initial times of the lights on

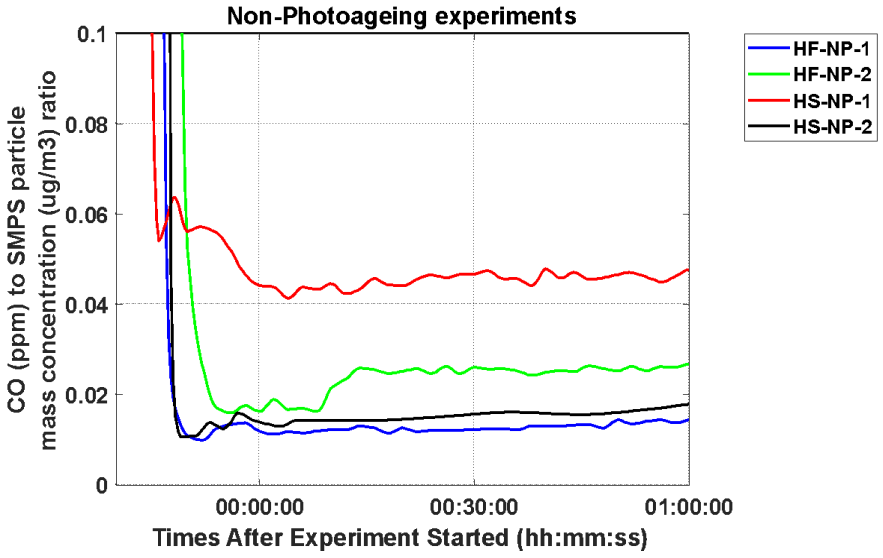


**(a)**

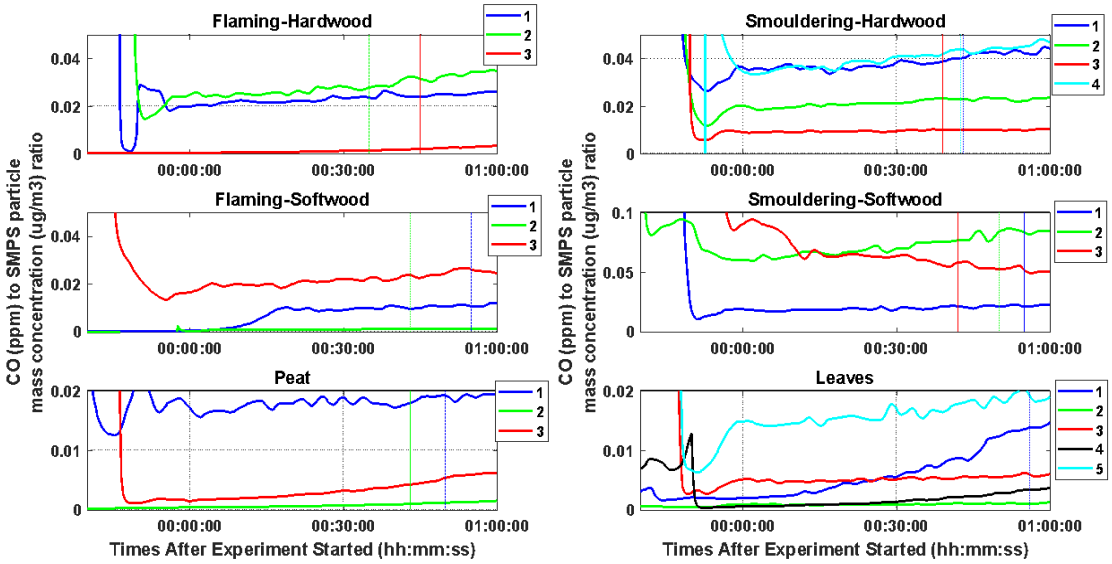


**(b)**

**Fig. S5** CO (ppm) to SMPS total particle mass (ug/m3) ratio of non-photoageing (a) and photo ageing (b) experiments; vertical red lines indicated the initial times of the light

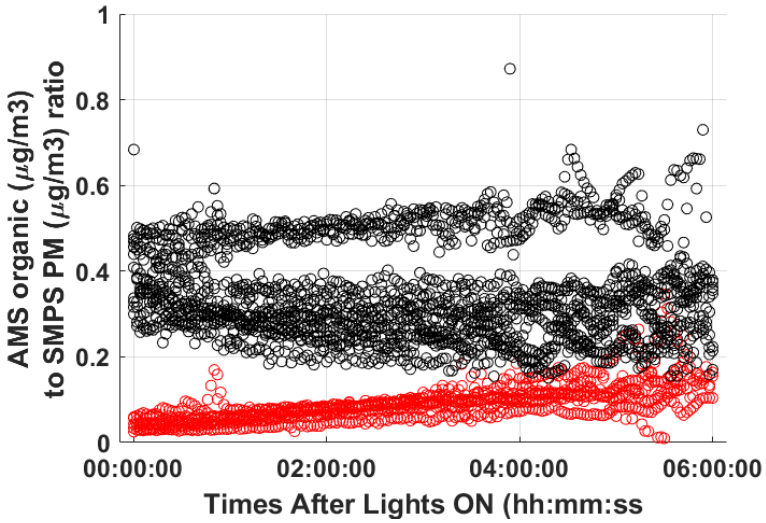


**Fig. S6.** AMS organic (ug/m3) to SMPS total mass (ug/m3) ratio of photoaging experiments, with red markers for flaming-photoaging experiments, whereas black markers for smouldering-photoaging experiments. Note: In this dataset, the time points when the thermodenuder was on have already been removed/excluded.

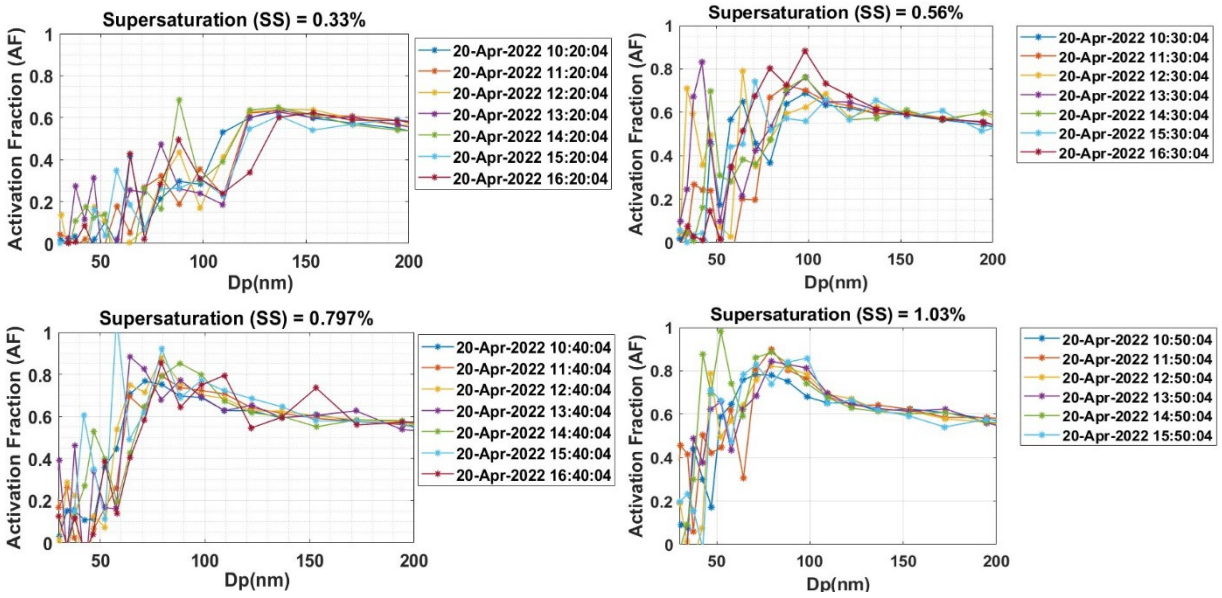


**Fig. S7.** Activation fraction, $F_A$, curves at different supersaturation and time points derived from CCNC measurements at four supersaturation, S, values in a smouldering hardwood photoaging experiment on 20$^{th}$ April 2022. No error bars displayed

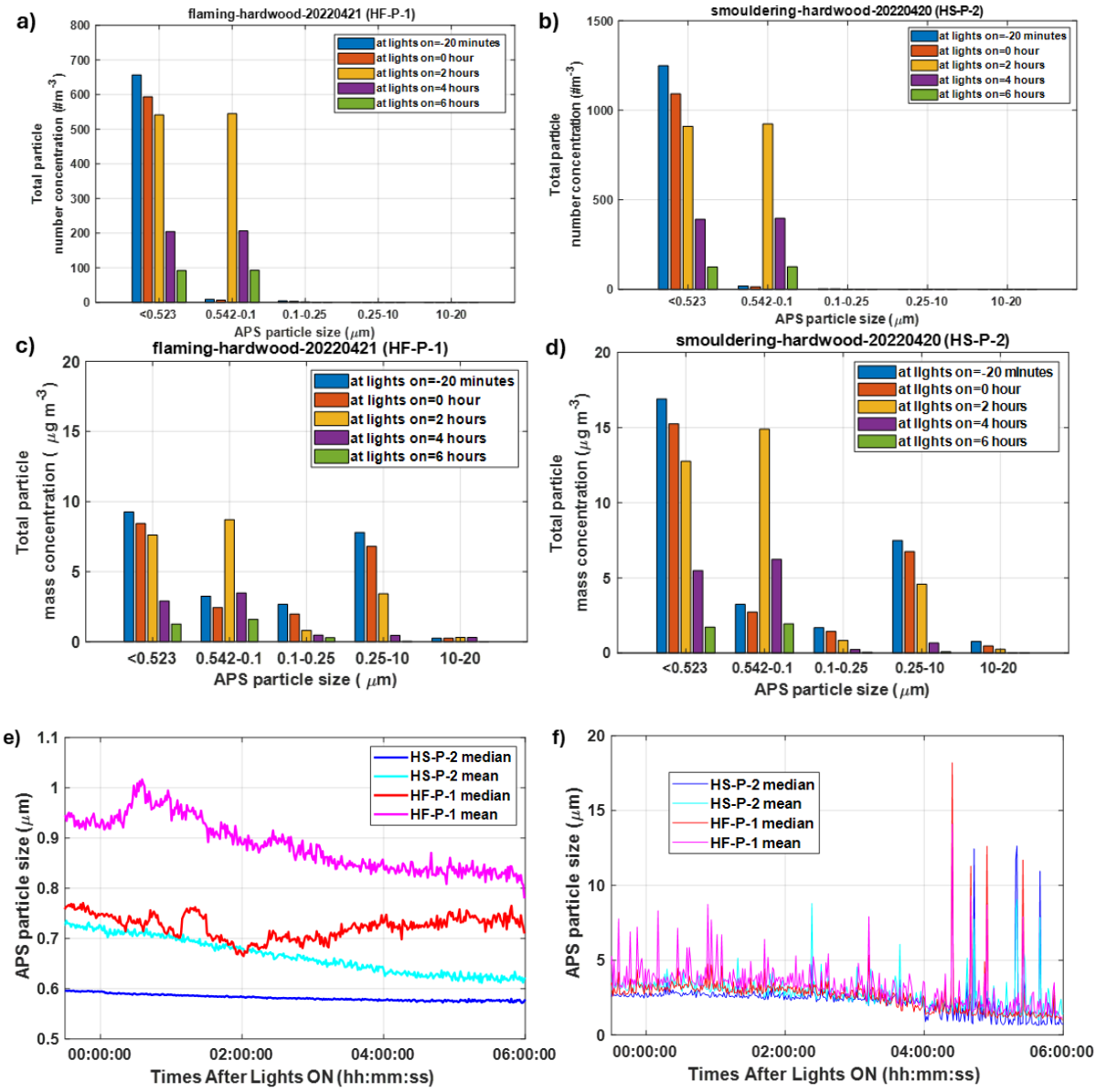


**Fig. S8.** Time point Aerosol Particle Sizer (APS) measurement graphs (**a-d**) of a flaming hardwood experiment on 21 April 2022 (F-HW-1) and a smoldering hardwood experiment on 20 April 2022 (S-HW-2), with time series Aerosol Particle Sizer (APS) mean and median values graphs from mass size distribution (left) and from number size distribution (right);

## Section 4: Evolution of NO and O3 mixing ratio during the biomass burning experiments

Direct flue measurements are capable of determination of properties of the gaseous and particulate components emitted as primary pollutants in the woodburning emissions. They are not able to reveal the transformations that these emissions would experience under atmospheric physical or chemical processing. Transformations will follow changes in environmental conditions after emission, including through physical drivers such as dilution, cooling and changes in RH. They may also occur as a result of chemistry driven by daytime or night-time oxidants. It is therefore necessary to conduct some kind of conditioning after emission and before measurement under the desired conditions. The MAC facility is well-suited to conduct photochemical and dark-ageing experiments by diluting and holding known concentrations from the woodsmoke under controlled dark or illuminated conditions. This is illustrated here by the evolution of NO mixing ratio and PM size distributions.

**Figure S9**, shows NO mixing ratio in the dark and illuminated experiments. The onset of illumination in the experiments in panel a) show the rapid perturbation towards photostationary state for all fuels. There is no equivalent perturbation in the dark experiments owing to the evidently more gradual changes in oxidative chemistry. Since the major consumption pathway for NO is the rapid bimolecular reaction with ozone (leading to $NO_2$ formation), it might be expected that the ozone concentration rapidly increased after the lights were illuminated. This is not apparent from the measurements in Figure 12.

However, there are a number of challenges in interpreting the time series of these gaseous componnets. $O_3$ measurements in this study used UV light absorption at 254 nm. Interferences at this wavelength may result from absorption by organic compounds in the gas phase wood burning emissions (Long R. W. et al 2021) and $O_3$ mixing ratios must be considered an upper limit. Moreover, it may be expected that illumination will initiate radical chemistry, leading to production of hydroperoxy ($HO_2$) and organic peroxy ($RO_2$) radicals, both of which may react with NO.

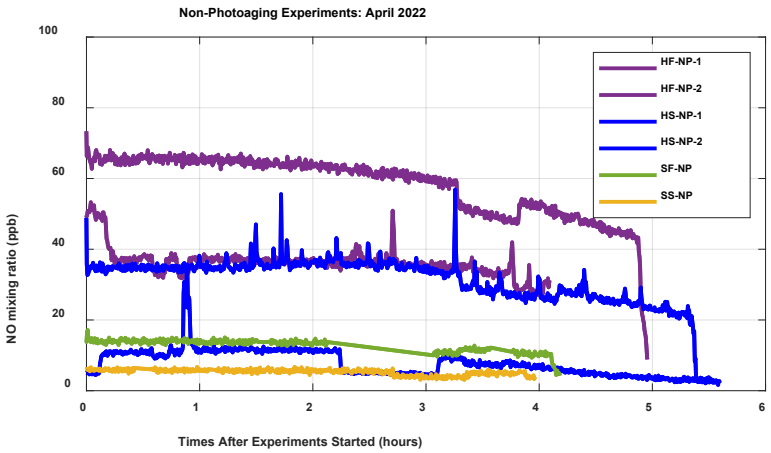


**(a)**

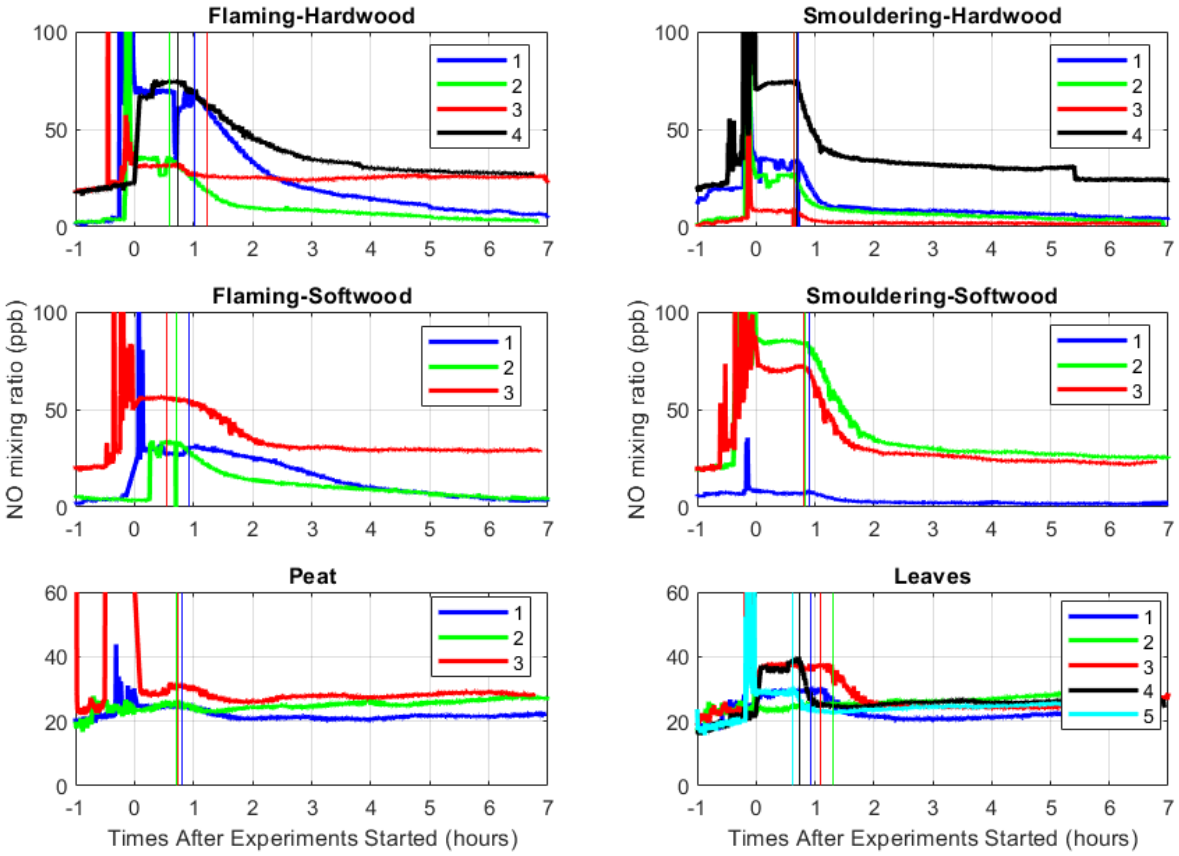


**(b)**

**Fig.S9.** NO measurements of at non-photoageing (a) and photoageing (b) experiments; vertical lines indicate the initial times of the lights on

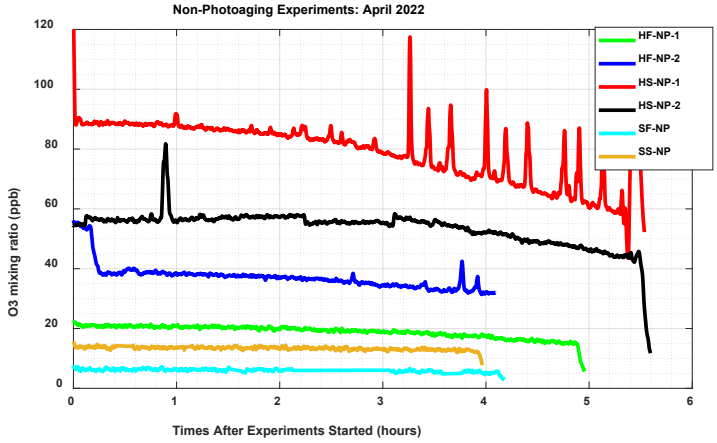


(a)

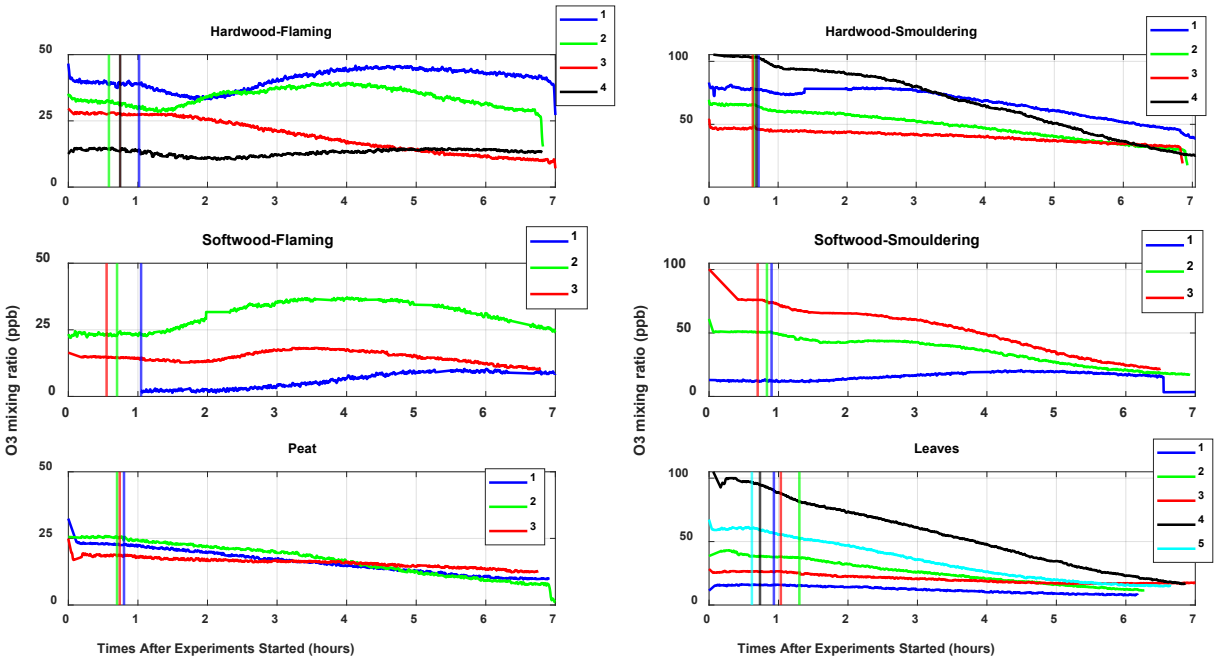


(b)

**Fig. S10** O3 measurements of at non-photoageing (a) and photoageing (b) experiments; vertical lines indicate the initial times of the lights on

In photostationary state (PSS), classically defined by the Leighton relationship (Leighton, P. A., 1961), the Leighton Ratio, $\Phi = j_{NO2}\,[NO_2]/(k_{NO+O3}[NO][O_3]) = 1$. The Leighton ratio time series graph can be looked at Supplementary Information, Figure S8. Reactions of NO with additional reaction partners such as $HO_2$ and $RO_2$ will lead to substantial deviation from photostationary state such that $\Phi$ will be significantly > 1 (Lien J and Hung H-M, 2021). Deviations from 1 can be seen in Fig. S8, with $\Phi > 1$ in two experiments. However, in most experiments $\Phi$ is persistently < 1. This can result from

i) consumption of $NO_2$ by reaction with photochemically produced OH to form $HNO_3$ (which will subsequently be lost to the walls) or
ii) production of $O_3$ or NO.

Photochemical production of both OH and $O_3$ may be expected and so both i) and ii) may be possible.

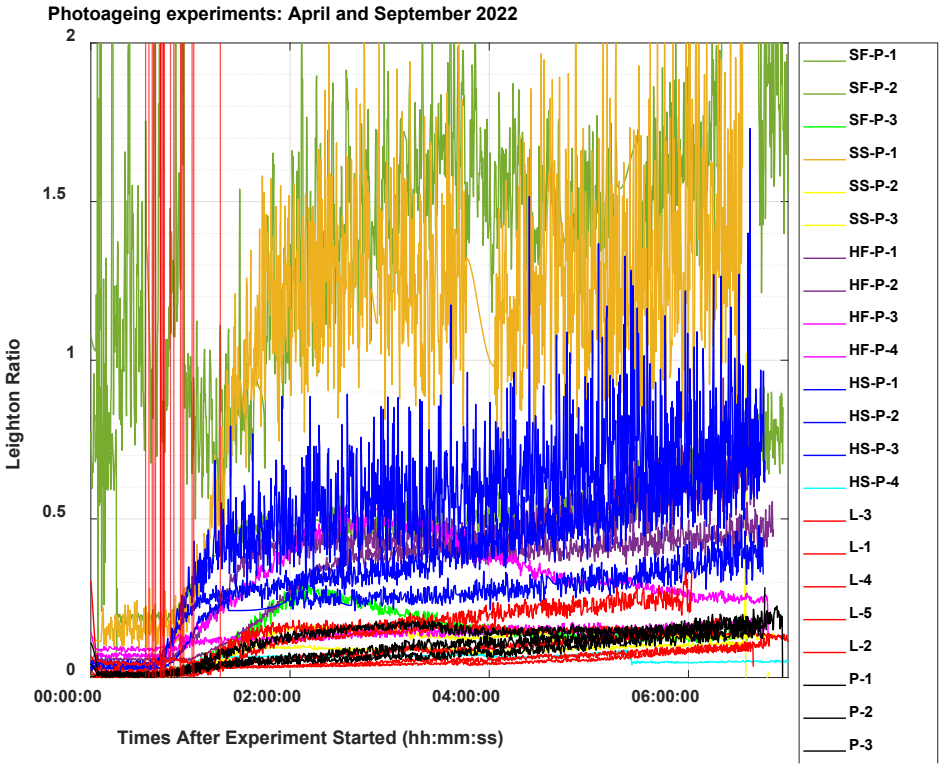


**Fig. S11. Leighton Ratio Time Series of Each Experiment**

**Section 5:** Additional Examples of Multi-Parameter Temporal Evolution of Biomass Burning Aerosol Properties

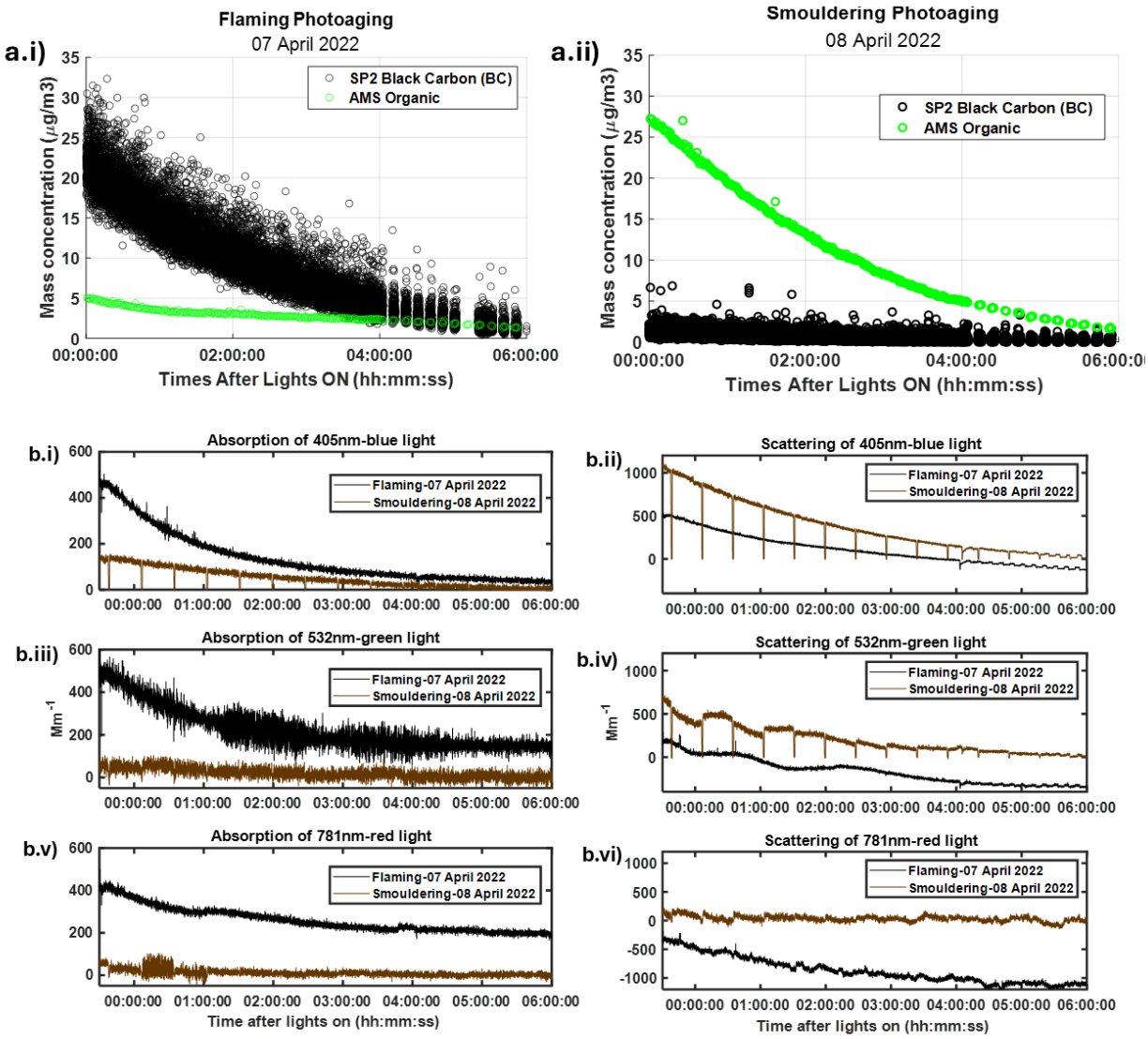


**Figure S12:** Graphs of the parallel and continuous time series measurements of c) AMS organic (orange and SP2 black carbon (blue) mass concentrations; d) absorption and scattering of the 3 wavelengths from the photoacoustic spectrometer, contrasting a flaming softwood (F-SW-1) and a smouldering softwood experiment (S-SW-1) on 7th April 2022 and 8th April 2022, respectively.

As shown in **Fig. S12**, the black carbon is clearly higher in flaming, leading to a much lower OC: BC ratio in the flaming experiment than in the smouldering experiment. Based on **Fig. S12.b**, it is clear that the total absorption was higher in the flaming experiment (07 April 2026) due to the high BC content, yet the scattering was higher in the smouldering experiment (08 April 2026) of the same fuel type. Black carbon is known as a component with high absorption across the infrared, visible, and ultraviolet regions (Liu F et al., 2019).